Physics of Plasmas

Electron-only reconnection and associated electron heating and acceleration in PHASMA

Cite as: Phys. Plasmas **29**, 032101 (2022); https://doi.org/10.1063/5.0082633
Submitted: 16 December 2021 • Accepted: 13 February 2022 • Published Online: 03 March 2022

Peiyun Shi, Prabhakar Srivastav, M. Hasan Barbhuiya, et al.

Electron-only reconnection and associated electron heating and acceleration in PHASMA

Cite as: Phys. Plasmas **29**, 032101 (2022); doi: 10.1063/5.0082633
Submitted: 16 December 2021 · Accepted: 13 February 2022 ·
Published Online: 3 March 2022

View Online Export Citation CrossMark

Peiyun Shi,[1,a] Prabhakar Srivastav,[1] M. Hasan Barbhuiya,[1] Paul A. Cassak,[1] Earl E. Scime,[1,b] M. Swisdak,[2] Cuyler Beatty,[1] Tyler Gilbert,[1] Regis John,[1] Matthew Lazo,[1] Ripudaman Singh Nirwan,[1] Mitchell Paul,[1] Ethan E. Scime,[1] Katey Stevenson,[1] and Thomas Steinberger[1]

AFFILIATIONS

[1]Department of Physics and Astronomy and the Center for KINETIC Plasma Physics, West Virginia University, Morgantown, West Virginia 26506, USA

[2]Institute for Research in Electronics and Applied Physics, University of Maryland, College Park, Maryland 20742, USA

Note: This paper is part of the Special Collection: Papers from the 63rd Annual Meeting of the APS Division of Plasma Physics.
Note: Paper NI1 4, Bull. Am. Phys. Soc. **66** (2021).
[a]Invited speaker. **Author to whom correspondence should be addressed:** peiyun.shi@mail.wvu.edu
[b]**Electronic mail:** earl.scime@mail.wvu.edu

ABSTRACT

Using incoherent Thomson scattering, electron heating and acceleration at the electron velocity distribution function (EVDF) level are investigated during electron-only reconnection in the PHAse Space MApping (PHASMA) facility. Reconnection arises during the merger of two kink-free flux ropes. Both push and pull type reconnection occur in a single discharge. Electron heating is localized around the separatrix, and the electron temperature increases continuously along the separatrix with distance from the X-line. The local measured gain in enthalpy flux is up to 70% of the incoming Poynting flux. Notably, non-Maxwellian EVDFs comprised of a warm bulk population and a cold beam are directly measured during the electron-only reconnection. The electron beam velocity is comparable to, and scales with, electron Alfvén speed, revealing the signature of electron acceleration caused by electron-only reconnection. The observation of oppositely directed electron beams on either side of the X-point provides "smoking-gun" evidence of the occurrence of electron-only reconnection in PHASMA. 2D particle-in-cell simulations agree well with the laboratory measurements. The measured conversion of Poynting flux into electron enthalpy is consistent with recent observations of electron-only reconnection in the magnetosheath [Phan *et al.*, Nature **557**, 202 (2018)] at similar dimensionless parameters as in the experiments. The laboratory measurements go beyond the magnetosheath observations by directly resolving the electron temperature gain.

I. INTRODUCTION

Magnetic reconnection is a universal process converting magnetic energy into thermal and kinetic energy of a plasma through the change of magnetic topology.[1] One important question about reconnection is what fraction of the energy released is delivered to the electrons and the ions. The distribution of energy plays a key role in looptop x-ray production in solar flares,[2] energetic particle injections following geomagnetic substorms,[3] and heating and acceleration of particles in tokamaks,[4–7] and has been studied observationally,[8–12] experimentally,[13–15] and theoretically or numerically.[16–19]

Although reconnection powers these various explosive phenomena at macroscopic scales, it is governed by processes at the microscopic, kinetic scale of ions and electrons.[20] In the typical reconnection picture, both electron and ion diffusion regions exist and define the region of magnetic reconnection and energy dissipation where magnetic field lines break and reconnect.[21] However, under some circumstances, e.g., in the turbulent magnetosheath, the characteristic scale lengths of the current sheets (the size of the reconnection region) are smaller than the ion kinetic scale.[22] With such an ordering of length scales, there is not sufficient space or time for ions to fully participate in the reconnection process. The result is that the cascade of energy to smaller length scales in magnetized turbulent plasmas is then mediated by electron-only reconnection rather than ion-coupled reconnection.[23]

The occurrence of electron-only reconnection has been confirmed in Earth's magnetosheath downstream of a quasi-parallel bow shock. Phan *et al.*[24] reported observations of Alfvén speed electron jets in opposite directions on either side of a reconnection X-point. Throughout the spacecraft trajectory through the magnetosheath, no

Alfvénic ion jets associated with the reconnection were observed. Phan *et al.* described these observations as definitive evidence of the occurrence of electron-only reconnection. Two-dimensional (2D) particle-in-cell (PIC) simulations have shown that ions start to decouple from the reconnection process when the island-to-island system size Δ drops below 40 times the ion kinetic scale.[25] The reconnection rate and electron outflow speed are significantly higher in 2D electron-only reconnection than in ion-coupled reconnection[25] and can be even higher in 3D electron-only reconnection.[26] Therefore, electron-only reconnection is an ideal candidate to explain small-scale energy dissipation in magnetized plasma turbulence[27–31] and near collisonless shocks.[32,33] However, little is known about how energy conversion during electron-only reconnection differs from fully ion-coupled reconnection.[12,34] Half the available magnetic energy was measured to be converted into bulk electron kinetic energy, and the other half was inferred to be transferred into electron thermal energy, but no direct measurement of electron heating was possible in the Phan *et al.* observations.[24] For those specific observations, the expected electron heating amount of several eV was smaller than the electron temperature measurement uncertainty, and the details of the electron velocity distribution function (EVDF) around the electron Alfvén speed are not accessible due to a low energy cutoff of the instrument.[35] No systematic observational or numerical studies of electron heating and acceleration in electron-only reconnection have been carried out to date.

The details of electron and ion velocity distribution functions (EVDFs and IVDFs) at the kinetic scale provided by satellite missions[36–38] and simulations[39] are essential to investigate energy conversion during magnetic reconnection, especially for the exploration of the relevant kinetic physics. However, complementary laboratory EVDF and IVDF measurements at the kinetic scale are still lacking.[40] Kinetic-scale measurements in laboratory experiments have enabled the identification of the electron diffusion region in reconnection.[41,42] Bulk electron and ion heating at the kinetic scale have been reported in laboratory reconnection studies[13,43,44] through electrostatic probe[45] and spectroscopic[46] measurements that do not resolve EVDFs. Thomson scattering diagnostics have been deployed in high-energy-density reconnection experiments.[47] However, they are usually operated in the coherent regime, where assumed models of the EVDFs are used to interpret the measured spectra. Therefore, those measurements are not a direct EVDF measurement.[48] Another diagnostic used in high-energy-density reconnection studies is an electron magnetic spectrometer, which directly measures EVDFs but in an *ex situ* manner.[49,50] Thus, fusion and heliospheric-relevant laboratory reconnection experiments have heretofore not directly measured EVDFs at kinetic scales.[51–53]

In this paper, we report details of the formation and diagnosis of two interacting flux ropes in the PHAse Space MApping (PHASMA) facility that result in electron-only magnetic reconnection and the direct measurements of EVDFs at the electron kinetic scale during this reconnection using an incoherent Thomson scattering diagnostic. To address electron energy conversion issues relevant to electron-only reconnection in the magnetosheath, we explore reconnection at normalized plasma parameters comparable to the Phan *et al.* observations[24] (see Table I). The ratio of the guide magnetic field B_g to the reconnecting field B_{recx} is relatively large, around 10, for both systems. The scale of difference between the ion and electron scales is ρ_s/d_e, where ρ_s is the ion gyroradius based on the ion sound speed and d_e is the electron inertial length. For both systems, this ratio falls in the range 20–30, similar to the well-studied parameter regime for fusion.[7] The electron plasma beta $\beta_e \leq 0.05$ in PHASMA is smaller than the 0.3 value in the magnetosheath, but both are much smaller than 1. Remarkably,[40] the observed electron heating characterized by the ratio $[\gamma/(\gamma-1)]n_e k_B \Delta T_e/(B_{recx}^2/\mu_0)$ is quite similar, 0.5–0.7, where n_e, ΔT_e, k_B, μ_0, and γ are electron density, electron temperature increase, Boltzman's constant, vacuum permeability, and the ratio of specific heats. The electron jet speeds V_e normalized to the electron Alfvén speeds V_{Ae} based on B_{recx} are in the range of 0.5–1, similar to those seen in the magnetosheath.

TABLE I. Plasma parameters for PHASMA and the magnetosheath electron-only reconnection event studied by Phan *et al.*[24]

	$\frac{B_g}{B_{recx}}$	$\frac{\rho_s}{d_e}$	$\boldsymbol{\beta_e}$	$\frac{[\gamma/(\gamma-1)]n_e k_B \Delta T_e}{B_{recx}^2/\mu_0}$	$\frac{V_e}{V_{Ae}}$
PHASMA	10–25	30	0.01–0.05	0.7	0.6–1
Magnetosheath	8	23	0.3	0.5	0.45

This paper is organized as follows: the experimental apparatus used to implement and diagnose magnetic reconnection between two flux ropes are described in Sec. II. The incoherent Thomson scattering system that provides direct measurements of EVDFs at the electron kinetic scale is also highlighted. In Sec. III, the dynamics of two interacting kink-free flux ropes is presented, where both push-type and pull-type reconnection are identified in a single discharge. The plasma parameters place the reconnection firmly in the electron-only regime. Electron heating is found to be localized around the separatrix in Sec. IV. The electron enthalpy gain and its dependence on the reconnecting and guide magnetic field strength are also reported. Non-Maxwellian EVDFs with electron beam structures are presented in Sec. V, revealing that electron acceleration arises from electron-only reconnection. In Sec. VI, a series of 2D PIC simulation specifically designed for this reconnection experiment successfully reproduce the observed electron heating results. A brief summary of this paper is given in Sec. VII.

II. EXPERIMENTAL APPARATUS

A. Flux rope experiments in PHASMA

PHASMA is a linear plasma facility capable of investigating various space plasma phenomena in the laboratory. PHASMA is equipped with both static helicon and pulsed gun plasma sources.[54,55] Figure 1 shows the experimental configuration used to initiate magnetic reconnection. The approach is similar to that used in previous linear reconnection devices.[56–58] Two 1-m long argon plasma columns embedded in a uniform axial magnetic field B_g are formed by plasma guns 1 and 2 (left side), separated by $\Delta = 60$ mm in the x direction. Subsequently, axial electrical current I_{bias} is drawn through the plasma columns by applying an electric potential between the plasma guns and a conical external anode (right side) to generate two flux ropes (blue columns). The conical external anode has a hole at its apex for diagnostic access. As the system of two flux ropes evolves (see Sec. III B), magnetic reconnection between their magnetic fields arises.[59]

Reconnection in PHASMA can be reasonably treated as quasi-2D case locally given the strong guide field used in these experiments, though some 3D effects are, indeed, expected considering the system

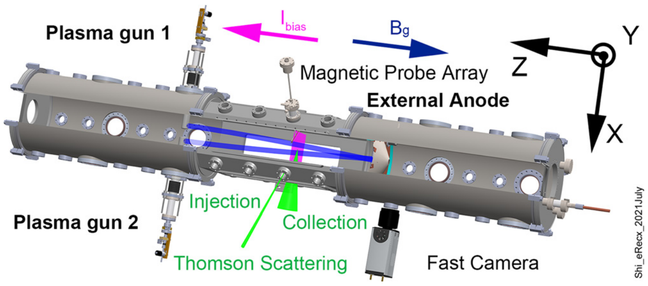

FIG. 1. The experimental apparatus for electron-only reconnection in PHASMA. Reconnection takes place between two flux ropes (blue columns), generated by two plasma guns (left) and an external anode (right). The key plasma diagnostics are a magnetic probe array, a fast camera, and Thomson scattering.

evolution along the out-of-plane direction, such effects as have been identified in other devices.[60] For this work, the suite of diagnostics focuses on one axial plane (pink color). A linear magnetic probe array composed of 17 $B_{r||}$ coils (along the probe shaft) and 17 $B_{r\perp}$ coils (perpendicular to the probe shaft) scans radially over 13 locations to map the repeatable 2D magnetic reconnection topology. For each radial location, four discharges are recorded. The 2D magnetic field vectors $\mathbf{B}_\perp = (B_x, B_y)$ at 221 locations are obtained from $B_{r||}$ and $B_{r\perp}$ measurements. The projection of the magnetic field lines on the xy plane is estimated from the lines of constant magnetic flux function ψ calculated using $\mathbf{B}_\perp = \hat{\mathbf{z}} \times \nabla\psi$. The flux function technique rigorously gives projections of magnetic field lines in 2D systems and is approximately valid for our quasi-2D experiments because of the relatively large B_g/B_{recx} ratio and small β_e.[59,61] A fast camera records the visible emission light intensity of plasmas escaping through the hole at the apex of the external anode, providing extra information about particle energization in the axial direction arising from the reconnection. The incoherent Thomson scattering diagnostic is implemented for the direct EVDF measurements in a similar axial plane to the magnetic probe array.

B. Thomson scattering system

While the details of the incoherent Thomson scattering system have been described elsewhere,[62] we highlight the relevant features enabling the electron heating and acceleration measurements in this study. The Thomson scattering diagnostic provides direct EVDF measurements along the differential wavevector direction $\vec{k} = \vec{k}_s - \vec{k}_i$, where $\vec{k}_i$ and $\vec{k}_s$ are the injection and scattering wavevectors, respectively, as shown in Fig. 2(a). In our experiment, the measured EVDFs are along the azimuthal direction $\theta = 22.5°$ in the xy plane. Several measures are taken to suppress the stray light at the wavelength of the injected laser beam, 532 nm. These include Brewster windows, planar baffles, and a beam dump. Taking advantage of the highly localized measurements possible with Thomson scattering, we are able to perform EVDF measurements at and below the electron inertial scale $d_e = 1.7$ mm. As is shown in the inset panel inside the magenta dashed rectangle, the beam profiler image shows that the overlapping volumes of the injection and collection beams are $\leq 0.5 \times 0.5 \times 1.0\,\mathrm{mm}^3$.

A small relative T_e measurement uncertainty 0.1 eV, i.e., $\leq 5\%$, achieved by our Thomson scattering system is critical for this experiment, given the expected electron heating amount is sub-eV.

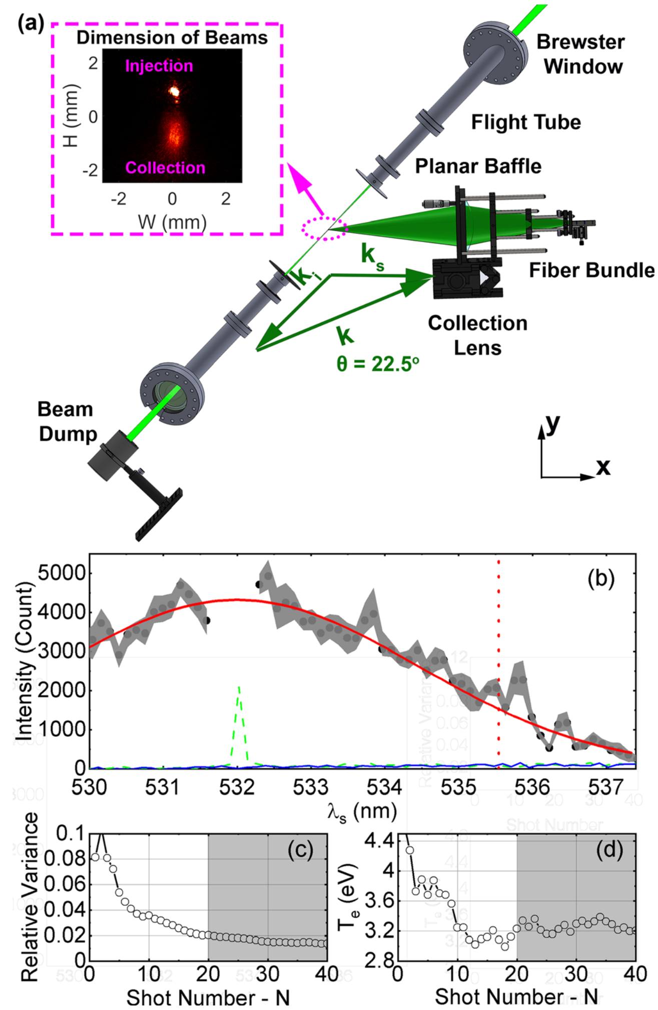

FIG. 2. (a) Schematics of the injection and collection optics of the Thomson scattering system. The measurement wavevector $\vec{k}$ is shown as the green arrow with an azimuthal angle of 22.5°. Shown inside the magenta dashed rectangles are the dimensions of the injection and collection beams as imaged with a beam profiler (before they overlap at the measurement location). (b) An example Thomson scattering spectrum (black points and shaded errorbar). The resultant Maxwellian fit is plotted as the red line with a vertical red dashed line denoting the 1/e spectral width. Spectra of stray light (green dashed line) and plasma self-emission light (blue line) are also included. (c) and (d) Relative variance of spectral intensity and fitted T_e values as a function of shot number N. The gray shading indicates the region where Thomson scattering measurements have stabilized.

Figure 2(b) shows an example Thomson scattering spectrum (black dots) obtained by accumulating spectra from 40 repeatable discharges. For reference, the spectrum of the stray light is plotted as the green dashed line, and the intensity of self-emission light from flux ropes is negligible as shown by the blue line. The red solid line presents the fitted Maxwellian profile with the vertical red dashed line denoting the fitted 1/e spectral width, resulting in $T_e = 3.2$ eV. To estimate the errorbar of the T_e measurement, we plot the T_e values derived via Maxwellian fits to the spectra accumulated from the first N repeatable discharges against the shot number N in Fig. 2(c). At the same time, the standard deviation of the raw spectra accumulated from the first N shots from the fitted Maxwellian spectra is calculated as a relative variance and is shown in Fig. 2(d). The T_e values settle down to around 3.2 eV after 10–20 shots, while the relative variance trace passes a "knee" and flattens out to around 0.02 for $N \geq 20$. Therefore, we use the standard deviation of T_e values for $N = 20$–40 as the uncertainty in the T_e measurements, 0.1 eV in this case. The gray shading around the data points in Fig. 2(b) shows the variance of the Thomson scattering spectrum intensity at each wavelength for shots $N = 20$–40.

III. EXPERIMENTAL PLATFORM OF ELECTRON-ONLY RECONNECTION

A. Kink-free operation regime

Experimentally, two requirements have to be satisfied to enable the study of electron heating and acceleration during electron-only reconnection in PHASMA. First, the magnitude of electron heating ΔT_e caused by magnetic reconnection should be larger than the uncertainty in the T_e measurements, so we can obtain statistically significant results. For our experiment, at a plasma density of $n_e = 1 \times 10^{19}\ \mathrm{m}^{-3}$, $\Delta T_e = 0.2$ eV requires that the reconnecting magnetic field B_{recx} is at least 9 G assuming the entire available magnetic energy goes into electrons. Second, the reconnection experiments should be very repeatable because 40 Thomson scattering spectra are normally needed to construct a single EVDF. However, the kink instability, which reduces the repeatability of our experiments, limits the achievable B_{recx} to about 10 G.[54] As is shown in Fig. 3(a), when the bias current reaches the kink threshold, 180 A (black dashed line), clear kink instabilities that appear as large fluctuations in the azimuthal magnetic field B_θ oscillations [black line in Fig. 3(b)] arise. Note that most previous linear reconnection experiments were operated in a regime with strong kink instabilities.[56,63] Here, we eliminate kink instability effects in the magnetic reconnection experiment by shortening the discharge period to be less than one axial Alfvén time. When the discharge period is reduced to 1% of previous experiments,[54] 100 μs, no significant kink instabilities are observed, see red lines in Fig. 3.

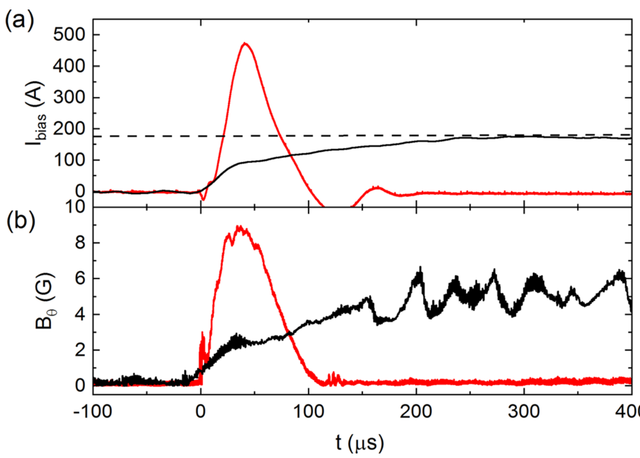

FIG. 3. (a) The bias current I_{bias} and (b) azimuthal magnetic field B_θ as a function of time. The black line is for the 10 ms discharge similar to that used in previous experiments,[54] while the red line is for the 100 μs discharges used in these magnetic reconnection experiments.[40]

B. Dynamics of two interacting flux ropes

For the kink-free operational regime described in Sec. III A, the magnetic reconnection process becomes highly repeatable, and the typical magnetic field topology is easily measured. Figure 4 shows the temporal evolution of the magnetic field topology (black lines as contour lines of ψ) and derived axial current density $J_z = (\nabla \times \mathbf{B}_\perp)_z$ (overlaying color) for two interacting flux ropes. At $t = 5.0\ \mu$s, the two flux ropes are located at $x = \pm 3$ cm. As the bias current ramps up, the two flux ropes rotate clockwise (along the ion gyromotion direction) around their center of mass. Similar rotational behavior of two interacting flux ropes was observed in the Reconnection Scaling Experiment (RSX)[59] and Large Plasma Device (LAPD) devices[64] and was believed to be related to the growth of the kink instability. Here, we argue that the kink instability is not likely to be the cause of the rotation in PHASMA because the kink has not yet had time to develop in our relatively short discharge and because later in time, the flux ropes rotate counterclockwise as the bias current decreases. We also note that this rotation exists for single flux rope, though with smaller displacements. Its appearance in single flux rope studies excludes the mutual centrifugal force of $-J_z B_\theta$ as a possible reason for this rotation. At the same time, the two flux ropes approach each other radially due to the mutual attraction force. After $t = 25.0\ \mu$s, the two flux ropes bounce away from each other. This radial bouncing motion was also reported by Sun *et al.*,[59] and they argued it was caused by the restoring magnetic tension force arising from the twisting of axial guide field lines. Note that magnetic flux pileup could also cause the observed bouncing dynamics of the flux ropes.[56,65]

As noted previously, the two flux ropes start to rotate backward (counterclockwise in the electron gyromotion direction) when I_{bias} reaches its peak value at $t = 40\ \mu$s. This behavior suggests that neither the kink instability nor diamagnetic effects are responsible for the clockwise and counter-counterclockwise rotation of the ropes in PHASMA because neither effect could change rotation direction during a single discharge. It appears that the rotation is more likely related to inductive, dI_{bias}/dt, effects, e.g., self-inductance of each flux rope or mutual inductance between two interacting flux ropes. While radial merging and bouncing, and azimuthal rotation along the ion gyromotion direction have been observed in previous multiple flux rope experiments,[59,64] there are no reports of backward rotations in those experiments.

To investigate these dynamics more quantitatively, we characterize the kinematics of two flux ropes by tracking their J_z centroids. Figure 5(a) shows the temporal evolution of the bias current I_{bias} and its rate of change dI_{bias}/dt to highlight the possible role of inductive effects. As is shown in Fig. 4, the radial displacement ΔR is defined as the distance between the two centroids, while the azimuthal displacement $\Delta\theta$ is defined as the azimuthal angle of the line connecting two centroids. The displacements ΔR and $\Delta\theta$ as a function of time based on the temporal evolution of magnetic field topology are plotted in Fig. 5(b). The radial velocity $v_R = d\Delta R/dt$ and the angular velocity $\omega_\theta = d\Delta\theta/dt$ are derived and plotted in Fig. 5(c). For context, the typical radial $v_R \sim 1.5$ km/s and azimuthal velocities $v_\theta = \omega_\theta R \sim 1.8$ km/s are comparable to the ion sound speed $C_s = [\gamma k_B (T_e + T_i)/m_i]^{1/2} \approx 3$ km/s, where $\gamma = 5/3$ is chosen. The measurements suggest a simple relationship between angular velocity and the rate of change of the bias current,

$$\omega_\theta \propto \frac{dI_{bias}}{dt}. \tag{1}$$

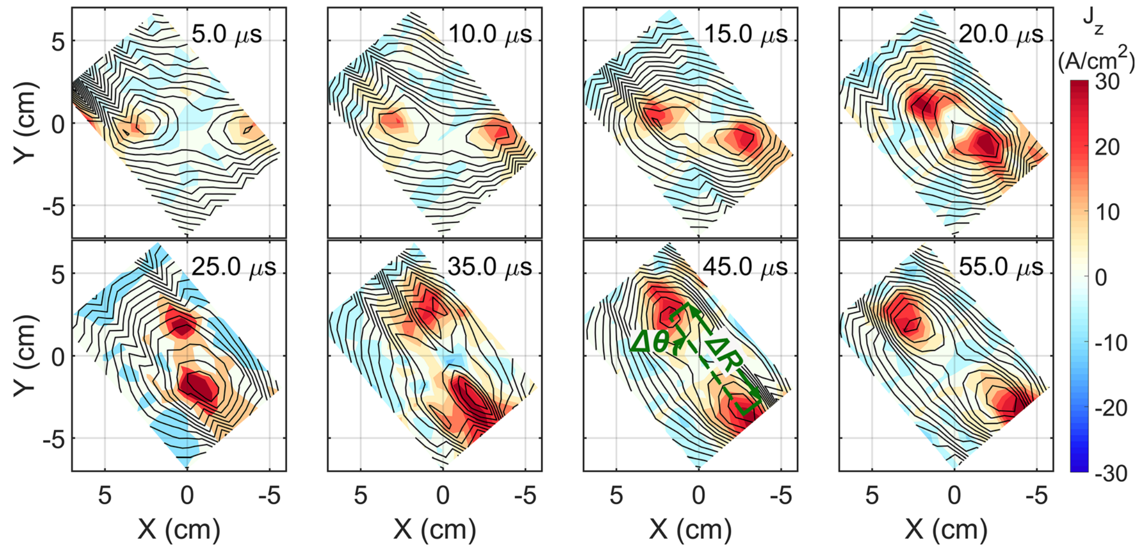

FIG. 4. The temporal evolution of the perpendicular magnetic field $\mathbf{B}_\perp$ (black lines) and axial current density J_z (overlaying color). The definitions of radial and azimuthal displacements ΔR and $\Delta\theta$ are denoted at $t = 45\,\mu$s.

The clear observation of this simple proportional dependence and observations of both clockwise and counterclockwise rotation during a single discharge are possibly enabled by the larger current ramp up and ramp down rates used in PHASMA $dI_{bias}/dt = 20$ A/μs compared to the typical values of 2 A/μs in RSX[66] and 0.7 A/μs in LAPD.[64] While the specific mechanism that drives the rotation is still a subject of investigation, the measurements clearly point to inductive effects playing a critical role.

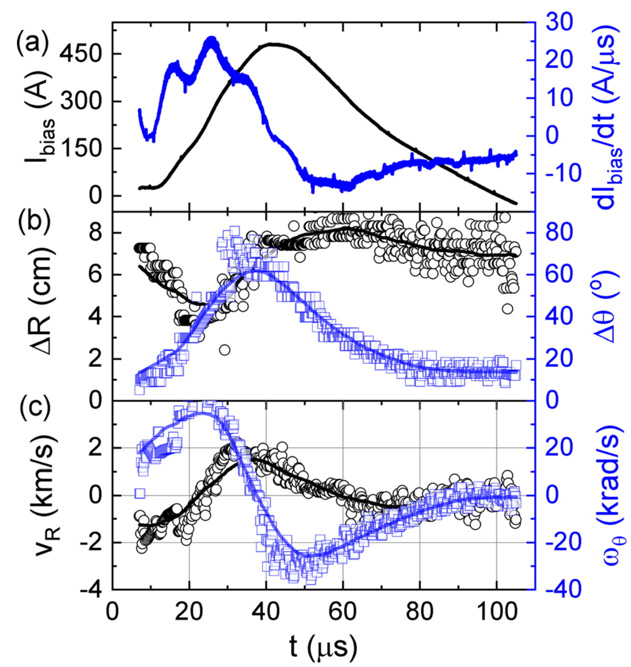

FIG. 5. (a) Time histories of the bias current I_{bias} and its rate of change dI_{bias}/dt, (b) radial displacement ΔR and azimuthal displacement $\Delta\theta$ of the flux ropes, and (c) radial velocity v_R and angular velocity ω_θ of the flux ropes.

C. Push and pull type reconnection

In Secs. III and IV, we focus on the magnetic reconnection that occurs between two flux ropes. It takes place on a spatially and temporally microscopic (mm-scale and μs-duration) process, far smaller than the macroscopic dynamics described above (cm-scale and 100 μs-duration). During a single discharge, we are able to identify the occurrence of magnetic reconnection twice. Figure 6(a) shows an occurrence of push-type reconnection at $t \approx 8\,\mu$s, where the two flux ropes approach each other (magenta arrows) and the magnetic field lines meet at the X-point, and reconnect and newly reconnected magnetic field lines are ejected outward (green arrows). In this case, the private magnetic flux of each single flux rope is combined into public flux shared by the two flux ropes.[67] At a later time $t \approx 49\,\mu$s, when the bias currents ramp down, the public magnetic flux changes back to the private flux of each rope during pull-type reconnection. As is shown in Fig. 6(b), the magnetic field lines are convected toward the X-point from the inflow region along the magenta arrows and then the reconnected field lines are slung toward the outflow regions along the green arrows. The occurrence of magnetic reconnection is experimentally confirmed by the appearance of reversed current density around the X-point, in light blue.[56,63] Typical X-type reconnection topology is also observed, especially during the pull-type phase.

Non-negligible reversed current density appears not only around the X-point but also around the outflow regions in the early push-type reconnection and the inflow regions in the later pull-type reconnection. We believe this is associated with the so-called "eddy current" or return current flowing in the surrounding tenuous plasma around the flux rope, which was also reported in similar experiments in RSX.[68,69] Indeed, such reversed current density also appears in our single flux

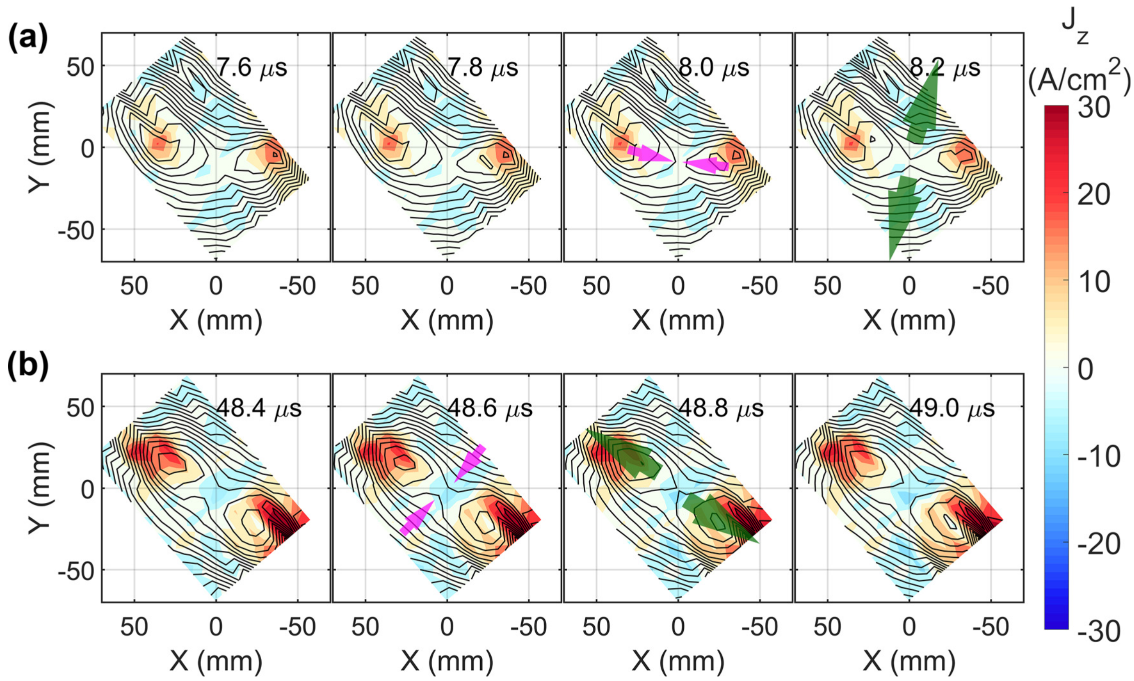

FIG. 6. (a) Push-type magnetic reconnection during the ramp up phase of the bias current at $t \sim 8\,\mu$s. (b) Pull-type magnetic reconnection in the ramp down phase of the bias current at $t \sim 49\,\mu$s. The magenta arrows indicate inflow directions, and green arrows the outflow directions.

rope experiments. However, the reconnection current around the X-point is only observed in two flux rope reconnection experiments. One clear difference is that the eddy current persists throughout the whole bias current interval, while the reconnection current only appears when the reconnection occurs.

Additional evidence of reconnection occurring twice in the same discharge comes from the intensity of emission light from plasma escaping through the hole located at the apex of external anode as recorded with a fast camera. Two phases of the magnetic reconnection, indicated by the reversal of J_z measured around $(x, y) = (3, -5)$ mm in Fig. 7(b), are highlighted by two yellow shaded areas, during the

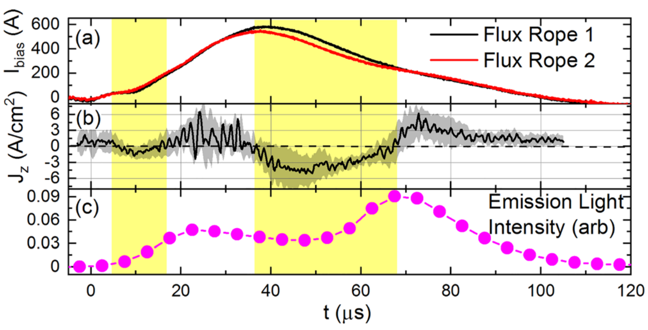

FIG. 7. (a) Bias current of two flux ropes, (b) axial current density measured around $(x, y) = (3, -5)$ mm, and (c) emission light intensity of the plasma escaping through the hole located at the apex of external anode as a function of time. The two yellow shaded areas highlight the occurrences of push and pull magnetic reconnection in a single discharge.

ramp-up and ramp-down phases of the bias current, see Fig. 7(a). As is shown in Fig. 7(c), there are two intervals of increased light emission that follow the intervals of reversed axial current density.[49,58] Bursts of increased light emission do not appear during single flux rope experiments. Since the emission increases across the entire $\sim$10 cm camera field of view in less than 5 μs, the axial propagation speed through the downstream region is faster than 20 km/s. The time delay between the increase in light emission and the peak of the reversed axial current density corresponds to a speed of 20–40 km/s, almost one order of magnitude larger than the ion sound speed 3 km/s but comparable to the electron drift speed $\sim$30 km/s in the reverse current that appears during reconnection. Thus, we conclude that the bursts of visible light emission are an indirect measurement of the axially accelerated electrons arising from the reconnection. These electrons are accelerated during reconnection, escape through the hole in the anode, and deposit energy in the background plasma downstream of the anode.

Given that the reversed J_z is larger (implying more available magnetic energy) and the collisionality is smaller (due to the smaller plasma density) during the pull reconnection, we focus on this phase of magnetic reconnection. The related parameters of the reconnection with reconnecting magnetic field $B_{recx} = 15$ G and guide field $B_g = 375$ G are listed in Table II. The current sheet thickness is $\delta = 5$ mm, and the reconnection system size defined by the distance between two O-points (centroids of two flux ropes) is $\Delta = 60$ mm. Both are larger than the electron inertial scale $d_e = 1.7$ mm, but far smaller than the scale at which ions fully couple to the reconnection, i.e., tens of the ion sound gyroradius,[25] $\rho_s = 42$ mm. Regarding relevant timescales, both the electron transit time through the current sheet $\tau = 0.1\,\mu$s and the overall reconnection duration of 20 μs are much larger than an electron

TABLE II. The comparison between spatial and temporal scales of the reconnection system and those of electrons and ions, suggesting the electron-only reconnection regime in PHASMA.

Scales	Electron	Reconnection system	Ion
Spatial	Electron inertial length $d_e = 1.7$ mm	System size $\Delta = 60$ mm; current sheet thickness $\delta = 5$ mm	Ion sound gyroradius $\rho_s = 42$ mm
Temporal	Electron gyroperiod $\tau_{ce} = 10^{-3}\ \mu$s	Electron transit time $\tau = 0.1\ \mu$s, duration 20 μs	Ion gyroperiod $\tau_{ci} = 70\ \mu$s

gyroperiod $\tau_{ce} = 10^{-3}\ \mu$s and much smaller than one ion gyroperiod $\tau_{ci} = 70\ \mu$s. Consequently, the ions have neither sufficient space nor time to fully participate in the reconnection process,[24] i.e., this reconnection is firmly in the electron-only regime. The collisionality of the plasma is another important physical parameter for reconnection. In these experiments, the rate of electron–neutral collisions is negligible compared to the rate of Coulomb collisions between electrons and ions. The mean free path of electron–ion collisions is estimated to be 13 mm, $\geq 2\delta$, and the characteristic collision time is about 0.02 μs, $\sim 0.2\tau$. Therefore, electrons experience at most a few collisions when transiting the current sheet, and the reconnecting plasma is marginally collisional.

IV. ELECTRON HEATING

With probe and spectroscopic measurements having established the electron-only nature of reconnection in PHASMA, we employ incoherent Thomson scattering and direct EVDF measurements to investigate the magnetic energy conversion, namely, the electron heating and acceleration, at the kinetic scale during electron-only reconnection.

A. Localized heating around the separatrix

For large guide field B_g, the electron heating arising from magnetic reconnection is expected to occur along the separatrix.[11,70] The expected quadrupolar electron heating pattern for finite guide field magnetic reconnection has been observed in Magnetic Reconnection Experiment (MRX).[34] Although the measurement location of our Thomson scattering measurements is fixed in PHASMA, we perform spatial scans by simultaneously translating the two guns to move the entire reconnection topology along the x direction. Serendipitously, the Thomson scattering measurement locations, as shown by the green dots in Fig. 8(a), cover one entire separatrix at $t = 47\ \mu$s. For our guide field orientation, the electron temperature is expected to increase along this separatrix because the axial Hall magnetic field B_H induced by electron motion (curved blue arrow) is opposite to the guide field B_g, which forces an enhancement of the electron thermal pressure to compensate for the reduced magnetic pressure along this separatrix.[70]

Figure 8(b) shows EVDFs measured at $x = 7$ mm (black) and $x = 1$ mm (red) at $t = 47\ \mu$s. As in Fig. 2(b), each EVDF measurement is obtained by accumulating 40 spectra acquired at the same time in the discharge, and the color bands reflect the standard deviation of the last 20 accumulated spectra. The solid lines are Maxwellian fits to the EVDFs, and the vertical dashed lines denote the electron thermal speeds v_{Te} obtained from these fits. Figure 8(c) shows the dependence of the T_e values on the number of accumulated spectra. Typically,

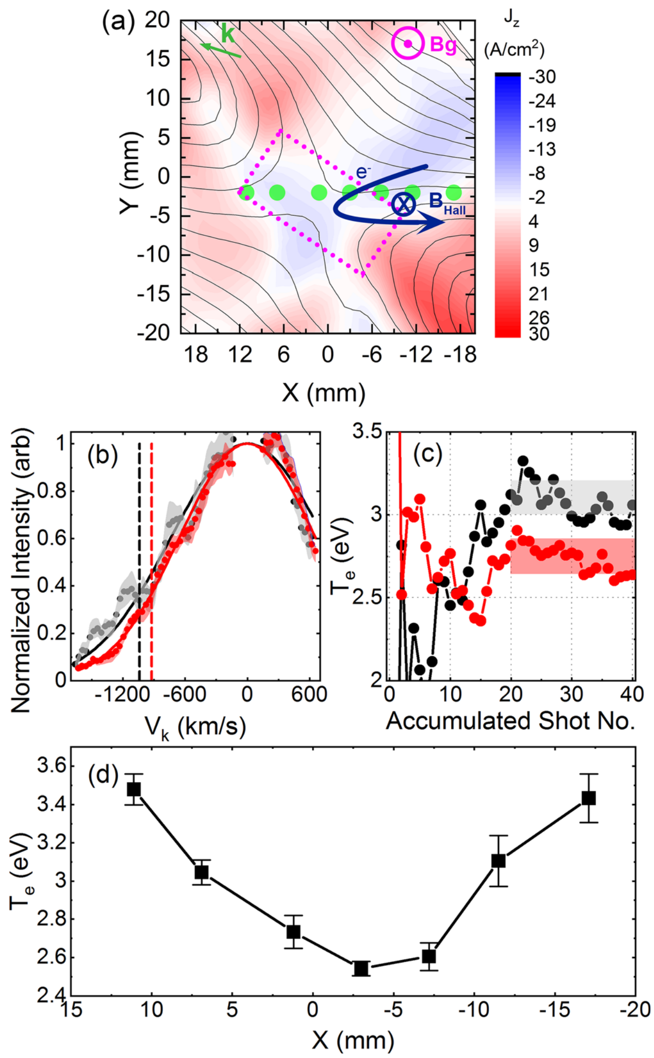

FIG. 8. (a) Magnetic field projections into the reconnecting plane (black lines) and axial current density (colors) at $t = 47\ \mu$s. The magenta dotted rectangular boundary is used to calculate energy fluxes. Green dots indicate accessible Thomson scattering measurement locations, while the green arrow at the upper left corner shows the measurement wavevector for the Thomson scattering system, $\vec{k}$. (b) EVDFs at $x = 7$ mm (black circles) and $x = 1$ mm (red circles). (c) The fitted T_e values as a function of accumulated shot number. (d) Electron temperature T_e as a function of x along the separatrix.

40 shots are required to reduce the relative uncertainty in T_e to be less than 10%, e.g., 3.1 ± 0.1 eV at $x = 7$ mm and 2.7 ± 0.1 eV at $x = 1$ mm. Figure 8(d) shows the change in the electron temperature T_e along the separatrix, x, direction. The electron temperature is clearly enhanced along the separatrix, increasing from 2.6 eV around the X-point at $x = 0$ mm to 3.4 eV downstream in either direction, an increase in nearly 30%.

Thanks to the natural rotation of the reconnection geometry as the flux ropes rotate, we access different azimuthal locations by firing the Thomson scattering diagnostics at different times in the discharge. Thus, we are able to measure EVDFs in the separatrix, inflow, and outflow regions. Figures 9(a)–9(c) show the reconnecting magnetic field topology (black lines) and axial current density (color) at $t = 42 \pm 1$, 46 ± 1, and 51 ± 1 μs, respectively. The measurement point indicated by red at $x = 11$ mm is located in the outflow region [red solid circle in panel (a)] at $t = 41$ μs. It moves to the separatrix region [red pentagon in panel (b)] at $t = 47$ μs and shifts back to the outflow region again at $t = 51$ μs. The corresponding temporal change in T_e obtained from the measured EVDFs at $x = 11$ mm is plotted as red points in Fig. 9(d), with three yellow bands denoting the times of panels (a)–(c). Clearly, the electron temperature is only enhanced in the separatrix region at $t = 47$ μs. Localization of the heating to the separatrix is verified with measurements at $x = -12$ mm (black points). That measurement location begins in the inflow region [black open circle in panel (a)] at $t = 42$ μs and moves to the separatrix region (black pentagons for $t = 46$ and 51 μs). Again, significant electron heating only appears when the measurement location is in the separatrix region. The electron temperature is lower in both the inflow and outflow regions. This localization of electron heating to the separatrix is consistent with previous reconnection studies with a finite B_g[11,34,70] and is reproduced in the 2D PIC simulations described in Sec. VI.

B. Electron enthalpy gain

Following the convention used in numerical simulations[16] and satellite observations,[9] we define the magnitude of electron heating ΔT_e as the difference between a local T_e measurement and the temperature in the inflow region. Figure 9(d) shows $T_e = 2.7 \pm 0.1$ eV in the inflow region, and it peaks at $T_e = 3.5 \pm 0.1$ eV around the separatrix. Given that the electron heating is expected to be non-uniform for a finite B_g, a truly rigorous study of the electron energy partition requires additional measurements throughout the reconnection region. Such measurements are planned for future investigations. Nevertheless, we can still provide complementary results to the magnetosheath observations by directly comparing the local electron enthalpy gain at a similar location relative to the X-point. In the work of Phan *et al.*,[24] the electron temperature enhancement was measured 3.5 km downstream, i.e., $1.8\,\delta$ away from the X-point. Correspondingly, we choose the T_e measurement at $1.8\,\delta = 9$ mm downstream of the X-point, 3.0 ± 0.1 eV. The ratio α is normally used to evaluate the energy conversion, $\alpha = \Delta H_e / S_{in}$, where ΔH_e is the electron enthalpy flux and S_{in} is the incoming Poynting flux. No electron density enhancement was observed around the separatrix in our experiment. Therefore, we define

$$\alpha = \frac{[\gamma/(\gamma-1)]k_B \Delta(n_e T_e)}{(B^2_{recx}/\mu_0)}. \tag{2}$$

In writing this expression, we tacitly assume that the system is adiabatic, so that $\gamma = 5/3$; this is a reasonable assumption because the guide field is large, and the distributions are typically close to Maxwellian. α is about 70% at $1.8\,\delta$ downstream of the X-point in PHASMA, which is comparable to the magnetosheath observation $\alpha \sim 50\%$. We also note that in the magnetosheath observation,[24] the α value was not directly measured but inferred because the associated electron temperature increase was too small to measure.

Different from the standard ion-coupled magnetic reconnection, in the electron-only reconnection, ions do not have sufficient space and time to participate in or respond to the reconnection process. Instead, they are limited to simply providing the neutralizing background. Electron only reconnection is mediated by whistler wave dynamics at electron scales, whereas the standard reconnection is controlled by Alfvén wave dynamics at ion scales.[71] That said, the reconnection rate can be larger in electron-only reconnection,[26] so can the electron flow speed.[25] Consequently, electron-only reconnection permits more magnetic energy to be converted into electron thermal and

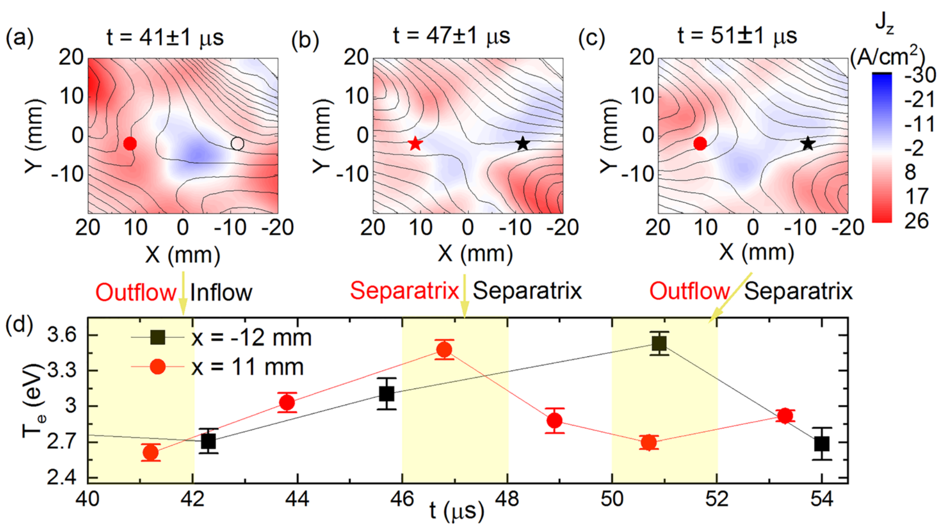

FIG. 9. (a)–(c) Magnetic field projections on the reconnecting plane (black lines) and axial current density (colors) at $t = 42 \pm 1$, 46 ± 1, and 51 ± 1 μs, respectively. Different measurement locations are denoted as points of different colors: red for $x = 11$ mm and black for $x = -12$ mm. Different shapes are for different regions: solid circles, blank circles, and solid stars for the outflow, inflow, and separatrix regions, respectively. (d) T_e at $x = 11$ mm (red) and $x = -12$ mm (black) as a function of time. Yellow shadings indicate the corresponding time periods of (a)–(c).

kinetic energy, as background ions are not expected to gain much energy.

Therefore, a smaller ratio α is expected in standard reconnection where ions participate in the reconnection. Fox *et al.*[34] reported a similar electron heating structure in reconnection with finite B_g in a much larger system $\Delta \simeq 5\,\rho_s$. As ions participate more in their reconnection process, the value for α was unsurprisingly smaller, about 23% at $1.8\,\delta$ away from the X-point. Our measured ratio of 70% is also considerably larger than the 14% reported by Yamada *et al.*[13] for zero guide field reconnection. As expected,[12] the conversion of magnetic energy into electron energy at kinetic scales is different in electron-only reconnection than in standard reconnection.

One important question regarding the conversion of magnetic into thermal energy is whether collisions or some other kinetic effects are the dominant processes for energy dissipation. To evaluate the relative importance of collisions, we consider the rectangle boundary of thickness $2\delta = 10$ mm and length $2L = 20$ mm around the X-point, shown as the magenta dotted rectangle in Fig. 8(a). The collisional Ohmic heating power per unit length out of the reconnection plane is calculated as $P_{Ohmic} = \eta J_z^2(2\delta \times 2L) \sim 0.03$ kW/m, where the Spitzer resistivity $\eta = 100\,\mu\Omega\,\text{m}$ is used and J_z near the X-point is used throughout the rectangle for simplicity. For the rate of electron enthalpy production per unit length in the out-of-plane direction P_H, we roughly estimate its magnitude based on local ΔT_e values, as our T_e measurements are limited to a single separatrix, and the heating on opposite separatrices is different in guide field reconnection.[70] Using the measured value $1.8\,\delta$ downstream for ΔT_e, we estimate $P_H = [\gamma/(\gamma-1)]n_e k_B \Delta T_e(2\delta \times 2L)/\tau \sim 2\,\text{kW/m}$. We note that the Spitzer prediction for η for a marginally collisional plasma and the derived J_z from magnetic field measurements are possibly underestimated, but the two-orders of magnitude difference between P_{Ohmic} and P_H is large enough to conclude that Ohmic heating is not the dominant process for magnetic to thermal energy conversion, and that other kinetic-scale processes must be responsible for the energy conversion. Indeed, the rate of magnetic enthalpy deposition per unit length in the out-of-plane direction $(B_{recx}^2/\mu_0) \times (2V_{in} \times 2L) = 3\,\text{kW/m}$ is large enough to account for the observed electron enthalpy gain.

C. Dependence on the reconnecting and guide field

Experimentally, we can verify that the observed electron heating comes from the reconnecting magnetic energy by varying the reconnecting magnetic field strength B_{recx}. Figure 10(a) shows that the measured electron enthalpy density gain $[\gamma/(\gamma-1)]n_e k_B \Delta T_e$ at a distance $1.8\,\delta$ from the X-point vs the reconnecting magnetic enthalpy B_{recx}^2/μ_0 as B_{recx} is varied from 10 to 20 G. The dashed line shows a linear fit with a slope of 0.8. The linear relationship demonstrates that the increased electron enthalpy comes from dissipation of the reconnecting magnetic field enthalpy during electron-only reconnection. Figure 10(b) shows the change in electron enthalpy density as a function of the ratio B_g/B_{recx} in the range of 10–25. No clear dependence of electron heating on the guide field strength is observed. This result is also reproduced in the 2D PIC simulations described in Sec. VI, since the reconnection rate is largely independent of guide field when B_g/B_{recx} is relatively large.[72,73]

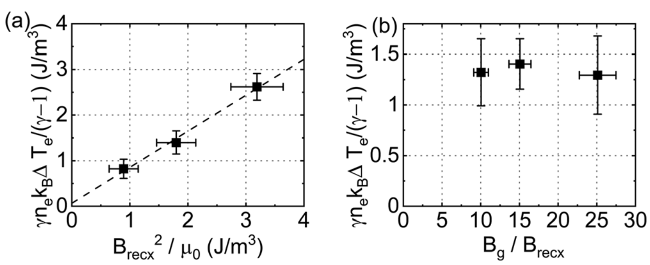

FIG. 10. (a) Measured electron enthalpy density increase $[\gamma/(\gamma-1)]n_e k_B \Delta T_e$ as a function of reconnecting magnetic enthalpy B_{recx}^2/μ_0 and (b) the ratio of guide field to reconnecting field B_g/B_{recx}. Reproduced with permission from Shi *et al.*, Phys. Rev. Lett. **128**, 025002 (2022). Copyright 2022 APS Publishing.

V. ELECTRON ACCELERATION AND NON-MAXWELLIAN EVDFS

Not only do the kinetic scale EVDF measurements provide insight into the process of electron heating during electron-only reconnection, electron acceleration is also observed through the appearance of non-Maxwellian features (oppositely directed electron beams) in the measured EVDFs. Figure 11(a) shows the EVDF as a function of V_k, the velocity component along $\vec{k}$, at $x = -3$ mm and $t = 55\,\mu$s. As is shown in Fig. 8(a), the $\vec{k}$ is at an angle of 22.5° and is mostly in the outflow direction. A clear electron beam of negative velocity appears

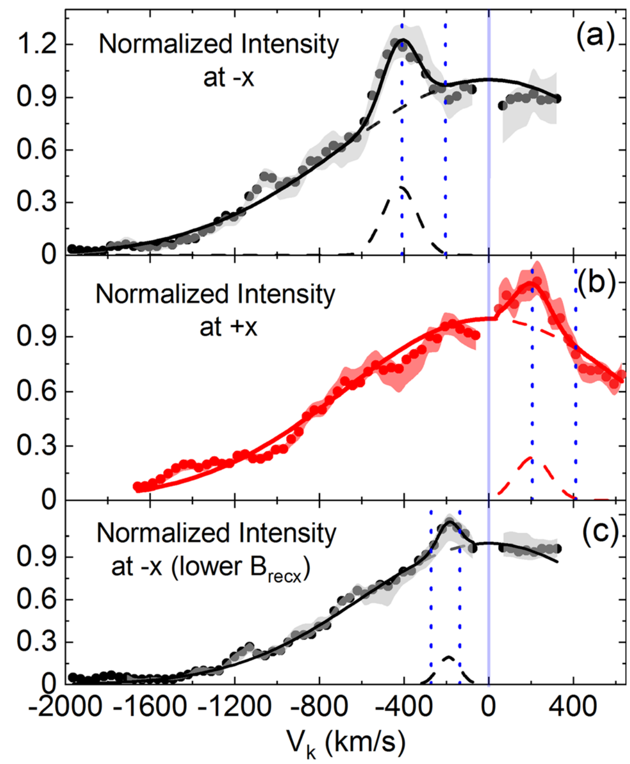

FIG. 11. EVDFs showing oppositely directed beams on either side of the X-point in the electron-only reconnection with $B_{recx} = 15$ G. (a) $x = -3$ mm (black circles) and (b) $x = 7$ mm (red circles). Dashed lines are Maxwellian fits for the individual bulk and beam electrons, and the solid line is their sum. The dotted vertical lines denote speeds of $V_{Ae}/2$ and V_{Ae}. (c) The EVDF measured at $x = -3$ mm for the $B_{recx} = 10$ G discharge.

TABLE III. The electron density n_e, temperature T_e, drift speed V_e, and enthalpy density of the bulk electron population and the electron beam. The ratios of these parameters between the electron beam and bulk electrons are shown in parentheses.

Populations	n_e	T_e	V_e	Enthalpy density
Bulk	1×10^{19} m^{-3}	2.8 eV	$\sim$0 km/s	4.5 J/m^3
Beam	4×10^{17} m^{-3} ($\times$0.04)	0.02 eV ($\times$0.01)	$\sim -$ 440 km/s	0.03 J/m^3 ($\leq \times$0.01)

superimposed on top of the bulk electron population. A composite fit (black solid line) based on the summation of two Maxwellian EVDFs is shown in Fig. 11(a). The total EVDF is well fit with a combination of a nearly stationary, warm bulk electron population, and a colder, much less dense, electron beam at a velocity of $V_k \simeq -440$ km/s. The speed of this electron beam is close to $V_{Ae} = 430$ km/s. Note that in the fits, the drift speed of the bulk Maxwellian is fixed at zero based on the observed structure of the EVDFs and the limited wavelength (velocity) range of the EVDF measurements. As is listed in Table III, the electron beam has a relative density of roughly $n_e^b \approx 0.04 n_e$ and an electron temperature of $T_e^b \approx 0.02$ eV $= 0.01 T_e$. The electron enthalpy density of the bulk electrons is about 4.5 J/m^{-3} while that of electron beam is negligible at 0.03 J/m^{-3}.

Figure 11(b) shows the EVDF on the other side of the X-point at $x = 7$ mm. The EVDF also exhibits a beam feature but with positive V_k. A fit to two Maxwellian distributions yields a flow speed of $V_k = +210$ km/s (half of V_{Ae}). To investigate if this feature is a reconnection outflow jet, we reduce the reconnecting magnetic field from 15 to 10 G. As is shown in Fig. 11(c), the electron beam speed at the same location as Fig. 11(a) drops to -180 km/s as V_{Ae} drops to 280 km/s. Thus, we measure oppositely directed electron beams at speeds $(0.6-1)V_{Ae}$ near the X-point, which is strong evidence of electron acceleration arising from electron-only reconnection.[24] Further from the X-point, the outflow decelerates, possibly a result of flow into the closed field lines of the flux ropes or because of collisions.

We note that in the Phan *et al.* observations,[24] the electron jets have been measured based on asymmetries in the EVDFs at large velocities because instrumental effects prevented measurements at velocities comparable to V_{Ae}. In other magnetosheath studies in which electron velocities comparable to V_{Ae} are resolvable, a well-defined, cold, electron beam moving in the outflow direction (reminiscent of the EVDFs observed in this experiment) is observed superimposed on a background electron population close to the separatrix.[74] Indeed, in early reconnection experiments at LAPD, it was also speculated that beam-like electrons are generated based on the observations of enhanced microwave emission near the plasma frequency.[75] The specific mechanism that generates these electron beams during electron-only reconnection in PHASMA is still under active investigation.

VI. 2D PIC SIMULATIONS

Motivated by the experimental measurements that show the reconnection system to be nearly symmetric, we perform simulations using the massively parallel PIC code p3d[76] that are 2D in position-space and 3D in velocity-space to compare with the measurements. In prior simulation studies,[25] electron-only reconnection physics was found to depend on the system size. Thus, we perform multiple simulations with a range of domain sizes $L_X \times L_Y = 80 \times 40\,\text{mm}^2$, $40 \times 20\,\text{mm}^2$, and $60 \times 30\,\text{mm}^2$. For the rest of this manuscript, we report findings from the $60 \times 30\,\text{mm}^2 = 35.25\ d_e \times 17.63\, d_e$ simulation because the X-point and O-point separation in the simulation when it achieves steady-state is close to the experimentally determined separation Δ. We find that the electron temperature gains are similar in all three domain size simulations, indicative of independence of electron temperature gains on the system size.

`p3d` uses a relativistic Boris stepper[77] to step particles forward in time and a trapezoidal leapfrog method[78] to step electromagnetic fields forward in time with a time step smaller than that of the time step of particles. In all our simulations, the divergence of the electric field $\vec{E}$ is cleaned by enforcing $\nabla \cdot \vec{E} = \rho/\epsilon_0$, where ρ is the net charge density, every ten-particle time-steps using the multigrid technique.[79]

Unlike the experiment, the simulation employs periodic boundary conditions. However, as we are studying the region very close to the X-point, the dissimilarities in the boundary conditions are inconsequential at these length-scales. At initialization, there are two 1D current sheets with only electrons carrying the current. The reconnecting magnetic field is $B_X = B_{recx}\{\tanh[(Y - 0.25L_Y)/w_0] - \tanh[(Y - 0.75L_Y)/w_0] - 1\}$ with the asymptotic reconnecting field strength far upstream of the X-point $B_{recx} = 15$ G and initial current sheet thickness $w_0 = 1.25$ mm. Initially, a uniform guide field $B_g = 25\, B_{recx} = 375$ G is employed. At initialization, electron and ion densities follow $n(Y) = n_{CS}\{\mathrm{sech}^2[(Y - L_Y/4)/w_0] + \mathrm{sech}^2[(Y - 3L_Y)/4w_0]\} + n_{up}$. Here, the asymptotic upstream density is $n_{up} = 1 \times 10^{13}$ cm^{-3} and the peak density of the current sheet is $n_{CS} = B_{recx}^2/[8\pi k_B(T_e + T_i)] = 0.2\, n_{up}$ with the initial electron T_e and ion T_i temperatures of 2.45 and 0.49 eV, respectively. The experimental system guides the selection of these parameters. The speed of light c is an unrealistic value of $c = 4.4 \times 10^6$ m/s $= 10\ c_{Ae,recx}$, where $c_{Ae,recx} = B_{recx}/(\mu_0 m_e n_{up})^{1/2}$ to significantly reduce the computational run time. As the system we are studying is non-relativistic, we note that our choice of c should not change the physics of the system. The time step $\Delta t = 2.67 \times 10^{-2}$ ns $= 7 \times 10^{-3}\, \Omega_{ce}^{-1}$, where $\Omega_{ce}^{-1} = eB_{recx}/m_e c^{-1}$ and e is the elementary charge. The simulation uses the realistic electron-to-argon ion mass ratio $m_e/m_i = 1/72\,900$, and the chosen grid-length $\Delta x = 3.9 \times 10^{-3}$ cm is much smaller the Debye length $\lambda_D \simeq \lambda_{Di} = (\varepsilon_0 k_B T_i / n_{up} e^2)^{1/2} = 9.9 \times 10^{-3}$ cm $= 0.06\ d_e$, which is the smallest length-scale in the system. There are 2048×1024 grid cells with 200 weighted particles per grid. A small initial magnetic field of the form $\delta B_X = -B_{pert} \sin(2\pi X/L_X) \sin(4\pi Y/L_Y)$ and $\delta B_Y = B_{pert} L_Y/(2L_X) \cos(2\pi X/L_X)[1 - \cos(4\pi Y/L_Y)]$ with $B_{pert} = 0.025$ is used to perturb the in-plane initial magnetic field, which seeds an X and O point pair in each of the two current sheets. We focus on the lower current sheet in the steady-state time interval since it does not produce secondary islands.

The 2D profile of electron temperature T_e at $t = 1.2\,\mu$ s is shown in Fig. 12(a), where we define the location of the X-point as (X_0, Y_0) and we plot the temperatures vs distance relative to that location. There is clear electron heating along one of the two separatrices - consistent

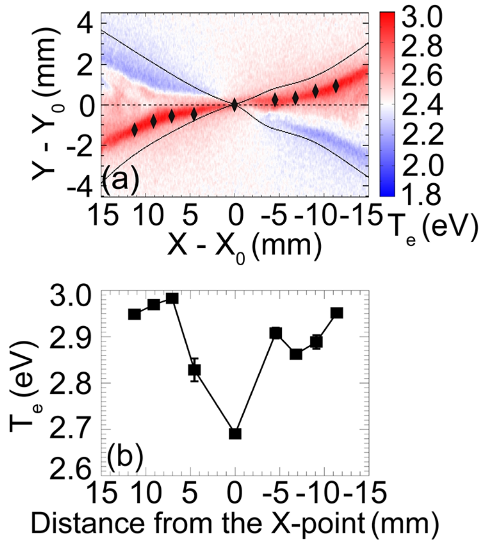

FIG. 12. (a) The 2D-profile of electron temperature from the PIC simulation. (b) T_e at the locations of the black diamonds in (a) as a function of distance from the X-point on both sides.

with previous strong guide field studies.[34,70] We note that the heating is localized to a narrow region of thickness $\simeq 1$ mm $\simeq 0.6\, d_e$ $\simeq 7\, \rho_e$ around the separatrix. A 1D plot of Fig. 12(a) at the locations marked by diamonds is shown in Fig. 12(b) and shows T_e as a function of distance from the X-point. The electron temperature T_e is smoothed over four cells to reduce noise, and the average T_e value is shown by black squares with error bars representing the standard deviation around this average value. We find that T_e steadily increases with distance away from the X-point, from $\sim$2.7 eV at the X-point to $\sim$3 eV peak value in the narrow hot separatrix region. These results are in excellent qualitative agreement with the experiment. Quantitatively, agreement is reasonable. We calculate that relative to the upstream temperature, the electron temperature increase at the peak of Fig. 12, ΔT_e, is $\sim$0.55 eV, which is also comparable to the experimental result of 0.8 eV. In the regions of interest motivated by the experiments, the simulations do not reproduce the measured EVDFs displayed in Sec. V. This suggests that 3D effects are likely to be essential to form the non-Maxwellian EVDFs observed in the experiments.

Motivated by Fig. 10(b), we perform additional simulations with initial guide field strengths of $B_g/B_{recx} = 10$ and 15. The initial electron and ion temperatures T_e and T_i, respectively, are the same as the experimental parameters. For the $B_g/B_{recx} = 15$ case, at $t = 0$, $T_e = 2.66$ eV and $T_i = 0.53$ eV. For the $B_g/B_{recx} = 10$ case, at $t = 0$, $T_e = 3.1$ eV, and $T_i = 0.62$ eV. In both these simulations, we find that the plasma density and reconnecting magnetic field profiles are similar to the $B_g = 25$ case, as expected. Data from a smaller simulation domain size (compared to the $B_g/B_{recx} = 25$ case) are used for further analysis for these two cases ($L_X \times L_Y = 40 \times 20\ \mathrm{mm}^2$) as bigger simulation domain runs produced secondary islands in both current sheets. We use a similar methodology as the experiments for obtaining the enthalpy density in the simulations, i.e., our chosen location lies about in the middle between the X-point and T_e peak location

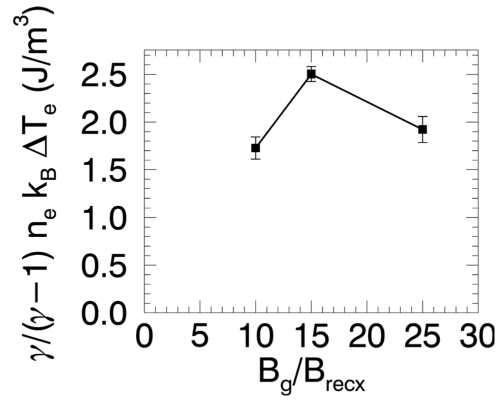

FIG. 13. Simulation analog of Fig. 4(b) showing the electron enthalpy density gain as a function of the ratio of guide field to reconnecting field strength.

taking place along the separatrix. As in Fig. 12(b), we smooth the T_e data over four cells to obtain mean values and error bars. We plot the increase in electron enthalpy density $\gamma/(\gamma-1)n_e k_B \Delta T_e$ as a function of B_g/B_{recx}, again assuming $\gamma = 5/3$, and the results are shown in Fig. 13. The simulation results show no strong dependence of electron heating on the guide field strength in this relatively large B_g/B_{recx} range, in reasonable agreement with the experiments, as shown in Fig. 10(b).

VII. CONCLUSION

In summary, electron-only reconnection experiments have been successfully conducted in the PHASMA facility. Two interacting kink-free argon flux ropes are generated to trigger magnetic reconnection as they merge. The kink-free regime is created by shortening the discharge period to be less than one axial Alfvén time. Naturally, the shorter discharge period introduces a larger rate of change in the bias current (10$\times$ previous experiments[59]). Possible induction effects on flux rope azimuthal dynamics are observed for the first time. Both push and pull type reconnection occur in a single discharge. The plasma parameters for these reconnection experiments are firmly in the electron-only regime with marginal collisionality. These conditions are comparable to the magnetosheath observations.[24]

Electron heating occurs predominantly along the separatrix, consistent with expectations for magnetic reconnection with a finite guide field.[70] The electron temperature during reconnection is found to be minimum around the X-point and increases continuously along the separatrix. The electron enthalpy gain is equal to 70% of the incoming Poynting flux, much larger than is reported for standard reconnection with more ion coupling ($\sim$20%).[34] By varying the reconnecting magnetic field strength B_{recx}, the electron enthalpy gain is found to be proportional to the reconnecting magnetic energy enthalpy. No clear dependence of electron heating on the guide field B_g is observed for these relatively large guide fields $(10-25)\,B_{recx}$. Notably, non-Maxwellian EVDFs composed of a warm bulk population and a cold beam are observed during electron-only reconnection. The electron beams are in opposite directions on either side of the X-point and their speed scales with the electron Alfvén speed based on the reconnecting magnetic field.

A series of 2D PIC simulations were completed for our experimental conditions, with a true mass ratio between ions and electrons and true guide field strength. The localized electron heating around the separatrix and the magnitude of electron heating in the simulations agree reasonably well with our measurements. Interestingly, the simulations do not reproduce the measured non-Maxwellian EVDFs, suggesting the cause is manifestly 3D. 3D PIC simulations are underway to understand the possible mechanisms responsible for these non-Maxwellian EVDFs. Upgrades of the Thomson scattering system are ongoing to enable multi-dimensional EVDF measurements in full 3D velocity phase space.

The electron-only reconnection experiments conducted in PHASMA successfully recreate, complement, and go beyond the relevant magnetosheath reconnection observations[24] because the electron heating is directly observed rather than being inferred and because they provide clear evidence that the electrons are accelerated to the electron Alfvén speed. Notably, the laboratory experiments also allow for the direct measurements of EVDF structures below the low velocity cutoff region of satellites, i.e., around the electron Alfvén speed. These experiments demonstrate that direct measurements of particle distribution functions at kinetic scales provide important context and insight in the study of electron-only magnetic reconnection in laboratory.

ACKNOWLEDGMENTS

We acknowledge fruitful discussions with Wondwossen Eshetu, Benoit Lavraud, Tai Phan, Prayash Sharma Pyakurel, and Shan Wang. This work was supported by Award Nos. NSF AGS 1602769; PHY 1804428, 1827325, and 1902111; NASA 80NSSC19M0146; and DoE DE-SC0020294. This research uses resources of NERSC, a DOE Office of Science User Facility supported by the Office of Science, under Contract No. DE-AC02-05CH11231.

AUTHOR DECLARATIONS

Conflict of Interest

The authors have no conflicts of interest to disclose.

DATA AVAILABILITY

The data that support the findings of this study are available from the corresponding author upon reasonable request.

REFERENCES

[1] M. Yamada, R. Kulsrud, and H. Ji, Rev. Mod. Phys. **82**, 603 (2010).
[2] T. G. Forbes, J. Geophys. Res. **105**, 23153, https://doi.org/10.1029/2000JA000005 (2000).
[3] J. Dungey, Phys. Rev. Lett. **6**, 47 (1961).
[4] S. von Goeler, W. Stodiek, and N. Sauthoff, Phys. Rev. Lett. **33**, 1201 (1974).
[5] A. W. Edwards, D. J. Campbell, W. W. Engelhardt, H. U. Fahrbach, R. D. Gill, R. S. Granetz, S. Tsuji, B. J. D. Tubbing, A. Weller, J. Wesson *et al.*, Phys. Rev. Lett. **57**, 210 (1986).
[6] E. Scime, S. Hokin, N. Mattor, and C. Watts, Phys. Rev. Lett. **68**, 2165 (1992).
[7] M. Yamada, F. M. Levinton, N. Pomphrey, R. Budny, J. Manickam, and Y. Nagayama, Phys. Plasmas **1**, 3269 (1994).
[8] J. Gosling, D. McComas, R. Skoug, and C. Smith, Geophys. Res. Lett. **33**, L17102, https://doi.org/10.1029/2006GL027188 (2006).
[9] T. D. Phan, M. A. Shay, J. T. Gosling, M. Fujimoto, J. F. Drake, G. Paschmann, M. Oieroset, J. P. Eastwood, and V. Angelopoulos, Geophys. Res. Lett. **40**, 4475, https://doi.org/10.1002/grl.50917 (2013).
[10] E. M. de Gouveia Dal Pino, P. P. Piovezan, and L. H. S. Kadowaki, Astron. Astrophys. **518**, A5 (2010).
[11] R. Wang, R. Nakamura, Q. Lu, W. Baumjohann, R. E. Ergun, J. L. Burch, M. Volwerk, A. Varsani, T. Nakamura, W. Gonzalez *et al.*, Phys. Rev. Lett. **118**, 175101 (2017).
[12] J. P. Eastwood, M. V. Goldman, T. D. Phan, J. E. Stawarz, P. A. Cassak, J. F. Drake, D. Newman, B. Lavraud, M. A. Shay, R. E. Ergun *et al.*, Phys. Rev. Lett. **125**, 265102 (2020).
[13] M. Yamada, J. Yoo, J. Jara-Almonte, H. Ji, R. M. Kulsrud, and C. E. Myers, Nat. Commun. **5**, 4774 (2014).
[14] M. Yamada, J. Yoo, and C. E. Myers, Phys. Plasmas **23**, 055402 (2016).
[15] J. Yoo, B. Na, J. Jara-Almonte, M. Yamada, H. Ji, V. Roytershteyn, M. R. Argall, W. Fox, and L.-J. Chen, J. Geophys. Res. **122**, 9264, https://doi.org/10.1002/2017JA024152 (2017).
[16] M. A. Shay, C. C. Haggerty, T. D. Phan, J. F. Drake, P. A. Cassak, P. Wu, M. Oieroset, M. Swisdak, and K. Malakit, Phys. Plasmas **21**, 122902 (2014).
[17] C. Haggerty, M. Shay, J. Drake, T. Phan, and C. McHugh, Geophys. Res. Lett. **42**, 9657, https://doi.org/10.1002/2015GL065961 (2015).
[18] J. Dahlin, J. Drake, and M. Swisdak, Phys. Plasmas **24**, 092110 (2017).
[19] Q. Lu, H. Wang, K. Huang, R. Wang, and S. Wang, Phys. Plasmas **25**, 072126 (2018).
[20] E. G. Zweibel and M. Yamada, Annu. Rev. Astron. Astrophys. **47**, 291 (2009).
[21] M. Hesse and P. A. Cassak, J. Geophys. Res. **125**, e2018JA025935, https://doi.org/10.1029/2018JA025935 (2020).
[22] I. Gingell, S. J. Schwartz, J. P. Eastwood, J. L. Burch, R. E. Ergun, S. Fuselier, D. J. Gershman, B. L. Giles, Y. V. Khotyaintsev, B. Lavraud *et al.*, Geophys. Res. Lett. **46**, 1177, https://doi.org/10.1029/2018GL081804 (2019).
[23] J. E. Stawarz, J. P. Eastwood, T. D. Phan, I. L. Gingell, M. A. Shay, J. L. Burch, R. E. Ergun, B. L. Giles, D. J. Gershman, O. L. Contel *et al.*, Astrophys. J. Lett. **877**, L37 (2019).
[24] T. D. Phan, J. P. Eastwood, M. A. Shay, J. F. Drake, B. U. Ö. Sonnerup, M. Fujimoto, P. A. Cassak, M. Øieroset, J. L. Burch, R. B. Torbert *et al.*, Nature **557**, 202 (2018).
[25] P. Sharma Pyakurel, M. A. Shay, T. D. Phan, W. H. Matthaeus, J. F. Drake, J. M. TenBarge, C. C. Haggerty, K. G. Klein, P. A. Cassak, T. N. Parashar *et al.*, Phys. Plasmas **26**, 82307 (2019).
[26] P. S. Pyakurel, M. A. Shay, J. F. Drake, T. D. Phan, P. A. Cassak, and J. L. Verniero, Phys. Rev. Lett. **127**, 155101 (2021).
[27] F. Califano, S. S. Cerri, M. Faganello, D. Laveder, M. Sisti, and M. W. Kunz, Front. Phys. **8**, 317 (2020).
[28] C. Vega, V. Roytershteyn, G. L. Delzanno, and S. Boldyrev, Astrophys. J. Lett. **893**, L10 (2020).
[29] G. Arró, F. Califano, and G. Lapenta, Astron. Astrophys. **642**, A45 (2020).
[30] N. F. Loureiro and S. Boldyrev, Astrophys. J. **890**, 55 (2020).
[31] R. Wang, Q. Lu, S. Lu, C. T. Russell, J. L. Burch, D. J. Gershman, W. Gonzalez, and S. Wang, Geophys. Res. Lett. **47**, e2020GL088761, https://doi.org/10.1029/2020GL088761 (2020).
[32] N. Bessho, L.-J. Chen, S. Wang, M. Hesse, and L. B. Wilson III, Geophys. Res. Lett. **46**, 9352, https://doi.org/10.1029/2019GL083397 (2019).
[33] N. Bessho, L.-J. Chen, S. Wang, M. Hesse, L. B. Wilson, and J. Ng, Phys. Plasmas **27**, 092901 (2020).
[34] W. Fox, F. Sciortino, A. v. Stechow, J. Jara-Almonte, J. Yoo, H. Ji, and M. Yamada, Phys. Rev. Lett. **118**, 125002 (2017).
[35] C. Pollock, T. Moore, A. Jacques, J. Burch, U. Gliese, Y. Saito, T. Omoto, L. Avanov, A. Barrie, V. Coffey *et al.*, Space Sci. Rev. **199**, 331 (2016).
[36] C. P. Escoubet, M. Fehringer, and M. Goldstein, Ann. Geophys. **19**, 1197 (2001).
[37] V. Angelopoulos, in *The THEMIS Mission*, edited by J. L. Burch and V. Angelopoulos (Springer, New York, 2009).
[38] J. L. Burch, T. E. Moore, R. B. Torbert, and B. L. Giles, Space Sci. Rev. **199**, 5 (2016).
[39] M. Hesse, T. Neukirch, K. Schindler, M. Kuznetsova, and S. Zenitani, Space Sci. Rev. **160**, 3 (2011).
[40] P. Shi, P. Srivastav, M. H. Barbhuiya, P. A. Cassak, E. E. Scime, and M. Swisdak, Phys. Rev. Lett. **128**, 025002 (2022).
[41] Y. Ren, M. Yamada, H. Ji, S. P. Gerhardt, and R. Kulsrud, Phys. Rev. Lett. **101**, 085003 (2008).

[42]J. Olson, J. Egedal, S. Greess, R. Myers, M. Clark, D. Endrizzi, K. Flanagan, J. Milhone, E. Peterson, J. Wallace *et al.*, Phys. Rev. Lett. **116**, 255001 (2016).
[43]Y. Ono, H. Tanabe, T. Yamada, M. Inomoto, T. Ii, S. Inoue, K. Gi, T. Watanabe, M. Gryaznevich, R. Scannell *et al.*, Plasma Phys. Controlled Fusion **54**, 124039 (2012).
[44]H. Tanabe, T. Yamada, T. Watanabe, K. Gi, K. Kadowaki, M. Inomoto, R. Imazawa, M. Gryaznevich, C. Michael, B. Crowley *et al.*, Phys. Rev. Lett. **115**, 215004 (2015).
[45]W. Fox, M. Porkolab, J. Egedal, N. Katz, and A. Le, Phys. Rev. Lett. **101**, 255003 (2008).
[46]M. R. Brown, Phys. Plasmas **6**, 1717 (1999).
[47]J. D. Hare, L. Suttle, S. V. Lebedev, N. F. Loureiro, A. Ciardi, G. C. Burdiak, J. P. Chittenden, T. Clayson, C. Garcia, N. Niasse *et al.*, Phys. Rev. Lett. **118**, 085001 (2017).
[48]A. L. Milder, J. Katz, R. Boni, J. P. Palastro, M. Sherlock, W. Rozmus, and D. H. Froula, Phys. Plasmas **28**, 82102 (2021).
[49]A. E. Raymond, C. F. Dong, A. McKelvey, C. Zulick, N. Alexander, A. Bhattacharjee, P. T. Campbell, H. Chen, V. Chvykov, E. D. Rio *et al.*, Phys. Rev. E **98**, 043207 (2018).
[50]J. Y. Zhong, J. Lin, Y. T. Li, X. Wang, Y. Li, K. Zhang, D. W. Yuan, Y. L. Ping, H. G. Wei, J. Q. Wang *et al.*, Astrophys. J. **225**, 30 (2016).
[51]Y. Liu, P. Shi, X. Zhang, J. Lei, and W. Ding, Rev. Sci. Instrum. **92**, 71101 (2021).
[52]G. G. Howes, Phys. Plasmas **25**, 055501 (2018).
[53]H. M. Milchberg and E. E. Scime, arXiv:1910.09084 (2019).
[54]P. Shi, P. Srivastav, C. Beatty, R. John, M. Lazo, J. McKee, J. McLaughlin, M. Moran, M. Paul, E. E. Scime *et al.*, Phys. Plasmas **28**, 32101 (2021).
[55]E. E. Scime, C. Beatty, D. Caron, T. Gilbert, A. Jemiolo, R. John, M. Lazo, J. McKee, M. Moran, R. S. Nirwan *et al.*, in *2021 International Conference on Electromagnetics in Advanced Applications (ICEAA)* (IEEE, 2021), p. 014.
[56]T. P. Intrator, X. Sun, G. Lapenta, L. Dorf, and I. Furno, Nat. Phys. **5**, 521 (2009).
[57]R. L. Stenzel and W. Gekelman, Phys. Rev. Lett. **42**, 1055 (1979).
[58]P. Shi, K. Huang, Q. Lu, and X. Sun, Plasma Phys. Controlled Fusion **61**, 125010 (2019).
[59]X. Sun, T. P. Intrator, L. Dorf, J. Sears, I. Furno, and G. Lapenta, Phys. Rev. Lett. **105**, 255001 (2010).
[60]W. Gekelman, T. DeHaas, C. Prior, and A. Yeates, SN Appl. Sci. **2**, 2187 (2020).
[61]W. Gekelman, T. De Haas, W. Daughton, B. Van Compernolle, T. Intrator, and S. Vincena, Phys. Rev. Lett. **116**, 235101 (2016).
[62]P. Shi, P. Srivastav, C. Beatty, R. S. Nirwan, and E. E. Scime, Rev. Sci. Instrum. **92**, 33102 (2021).
[63]W. Gekelman, T. DeHaas, P. Pribyl, S. Vincena, B. V. Compernolle, R. Sydora, and S. K. P. Tripathi, Astrophys. J. **853**, 33 (2018).
[64]B. Van Compernolle and W. Gekelman, Phys. Plasmas **19**, 102102 (2012).
[65]H. Karimabadi, J. Dorelli, V. Roytershteyn, W. Daughton, and L. Chacón, Phys. Rev. Lett. **107**, 025002 (2011).
[66]I. Furno, T. P. Intrator, G. Lapenta, L. Dorf, S. Abbate, and D. D. Ryutov, Phys. Plasmas **14**, 022103 (2007).
[67]R. Kulsrud, *Plasma Physics for Astrophysics* (Princeton University Press, 2005).
[68]J. von der Linden, J. Sears, T. Intrator, and S. You, Phys. Rev. Lett. **121**, 35001 (2018).
[69]A. Alt, C. E. Myers, H. Ji, J. Jara-Almonte, J. Yoo, S. Bose, A. Goodman, M. Yamada, B. Kliem, and A. Savcheva, Astrophys. J. **908**, 41 (2021).
[70]R. G. Kleva, J. F. Drake, and F. L. Waelbroeck, Phys. Plasmas **2**, 23 (1995).
[71]M. E. Mandt, R. E. Denton, and J. F. Drake, Geophys. Res. Lett. **21**, 73, https://doi.org/10.1029/93GL03382 (1994).
[72]M. Hesse, K. Schindler, J. Birn, and M. Kuznetsova, Phys. Plasmas **6**, 1781 (1999).
[73]P. L. Pritchett, J. Geophys. Res. **106**, 3783, https://doi.org/10.1029/1999JA001006 (2001).
[74]S.-C. Bai, Q. Shi, Q.-G. Zong, X. Wang, A. Tian, A. W. Degeling, C. Yue, I. J. Rae, Z.-Y. Pu, and S. Fu, J. Geophys. Res. **124**, 7494, https://doi.org/10.1029/2019JA026836 (2019).
[75]R. L. Stenzel, W. Gekelman, and N. Wild, J. Geophys. Res. **87**, 111, https://doi.org/10.1029/JA087iA01p00111 (1982).
[76]A. Zeiler, D. Biskamp, J. Drake, B. Rogers, M. Shay, and M. Scholer, J. Geophys. Res. **107**, SMP 6-1–SMP 6-9, https://doi.org/10.1029/2001JA000287 (2002).
[77]C. K. Birdsall and A. B. Langdon, *Plasma Physics Via Computer Simulation* (Taylor & Francis, 2004).
[78]P. N. Guzdar, J. F. Drake, D. McCarthy, A. B. Hassam, and C. S. Liu, Phys. Fluids B **5**, 3712 (1993).
[79]U. Trottenberg, C. W. Oosterlee, and A. Schuller, *Multigrid* (Academic Press, San Diego, 2000).